UC Davis
UC Davis Previously Published Works

Title

North Atlantic meltwater during Heinrich Stadial 1 drives wetter climate with more atmospheric rivers in western North America.

Permalink

https://escholarship.org/uc/item/37q3z7sv

Journal

Science Advances, 9(46)

Authors

Oster, Jessica
Macarewich, Sophia
Lofverstrom, Marcus
et al.

Publication Date

2023-11-15

DOI

10.1126/sciadv.adj2225

Peer reviewed

CLIMATOLOGY

North Atlantic meltwater during Heinrich Stadial 1 drives wetter climate with more atmospheric rivers in western North America

Jessica L. Oster[1]*, Sophia Macarewich[2], Marcus Lofverstrom[3], Cameron de Wet[1,4], Isabel Montañez[4], Juan M. Lora[5], Christopher Skinner[6], Clay Tabor[7]

Atmospheric rivers (ARs) bring concentrated rainfall and flooding to the western United States (US) and are hypothesized to have supported sustained hydroclimatic changes in the past. However, their ephemeral nature makes it challenging to document ARs in climate models and estimate their contribution to hydroclimate changes recorded by time-averaged paleoclimate archives. We present new climate model simulations of Heinrich Stadial 1 (HS1; 16,000 years before the present), an interval characterized by widespread wetness in the western US, that demonstrate increased AR frequency and winter precipitation sourced from the southeastern North Pacific. These changes are amplified with freshwater fluxes into the North Atlantic, indicating that North Atlantic cooling associated with weakened Atlantic Meridional Overturning Circulation (AMOC) is a key driver of HS1 climate in this region. As recent observations suggest potential weakening of AMOC, our identified connection between North Atlantic climate and northeast Pacific AR activity has implications for future western US hydroclimate.

INTRODUCTION

Atmospheric rivers (ARs) are ephemeral, concentrated pathways of atmospheric moisture transport that are responsible for the majority of poleward moisture transport in the midlatitudes (1, 2). When ARs reach the west coast of the United States (US), the interaction of the moisture-laden air with coastal and near-coastal mountains can lead to intense and substantial orographic precipitation that can alleviate drought but also induce flooding (3–6). The importance of ARs to the modern hydrologic budget of the semiarid western US has prompted numerous investigations into their role in past climate states, particularly during the Last Glacial Maximum (LGM) and ensuing deglaciation (7–9), an interval of marked regional hydroclimate changes as evidenced by the growth of pluvial lakes across the region (10).

Proxy records and climate model simulations have emphasized a pattern of increased wetness at the LGM in the southwestern US and increased aridity in the northwestern US that may have arisen from a southward shifted extratropical storm track, increased rainout over land due to stronger temperature gradients, reduced evaporation due to cooler temperatures, and an increase in southwesterly moisture transport from AR storms (7, 9, 11–13). However, substantial geochronologic and proxy data evidence demonstrates that (i) the timing of pluvial lake highstands and therefore potentially wetter climate conditions was temporally variable across the region (8, 14) and (ii) most of the presumably wettest conditions postdate the LGM (10, 15). Heinrich Stadial 1 [HS1; 18,000 to 14,700 years before the present (B.P.)] was a period of intense winter cooling and iceberg release into the North Atlantic (16). Many pluvial lakes in the Great Basin, a contiguous area of inward-draining watersheds extending from southeastern California north to central Oregon and east through northern Utah, reached highstands during some portion of HS1 (8, 15).

The mechanisms behind the wetness during HS1 have been investigated through model experiments and proxy record compilations. Comparison between proxies from across North America and the TraCE21K transient simulation of the last deglaciation found the strongest agreement in the sign of hydroclimate change in western North America where winter precipitation dominates the seasonal hydroclimate budget (17). However, TraCE21K only simulates minor upticks in boreal winter [December, January, and February (DJF)] precipitation in the western US (California and Nevada) between 16,000 and 15,000 years B.P. relative to the LGM (18), and in boreal fall [September, October, and November (SON)] precipitation between ~17,000 and 15,000 years B.P. (17), possibly due to its ice sheet configuration (19). In a set of idealized freshwater hosing experiments conducted under different orbital configurations, McGee et al. (8) found that the increased winter precipitation in western North America during Heinrich stadials was closely associated with southward displacement of the intertropical convergence zone (ITCZ) and intensification of the east-central Pacific Hadley circulation. They put forward a conceptual model suggesting that freshwater hosing changes the tropical circulation, which, in turn, helps intensify the subtropical jet, deepen the Aleutian Low, and draw AR-like subtropical moisture into western North America, including the Great Basin where pluvial lakes expanded (Fig. 1). However, the coarse resolution and idealized representation of Heinrich stadials in those simulations precluded a comprehensive understanding of the dynamics of HS1 hydroclimate and how ARs may have contributed to increased regional wetness at this time.

[1]Department of Earth and Environmental Sciences, Vanderbilt University, Nashville, TN, USA. [2]National Center for Atmospheric Research, Boulder, CO, USA. [3]College of Geosciences, University of Arizona, Tucson, AZ, USA. [4]Department of Earth and Planetary Sciences, University of California, Davis, Davis, CA, USA. [5]Department of Earth and Planetary Sciences, Yale University, New Haven, CT, USA. [6]Department of Environmental, Earth and Atmospheric Sciences, UMass Lowell, Lowell, MA, USA. [7]Department of Earth Sciences, University of Connecticut, Storrs, CT, USA.
*Corresponding author. Email: jessica.l.oster@vanderbilt.edu
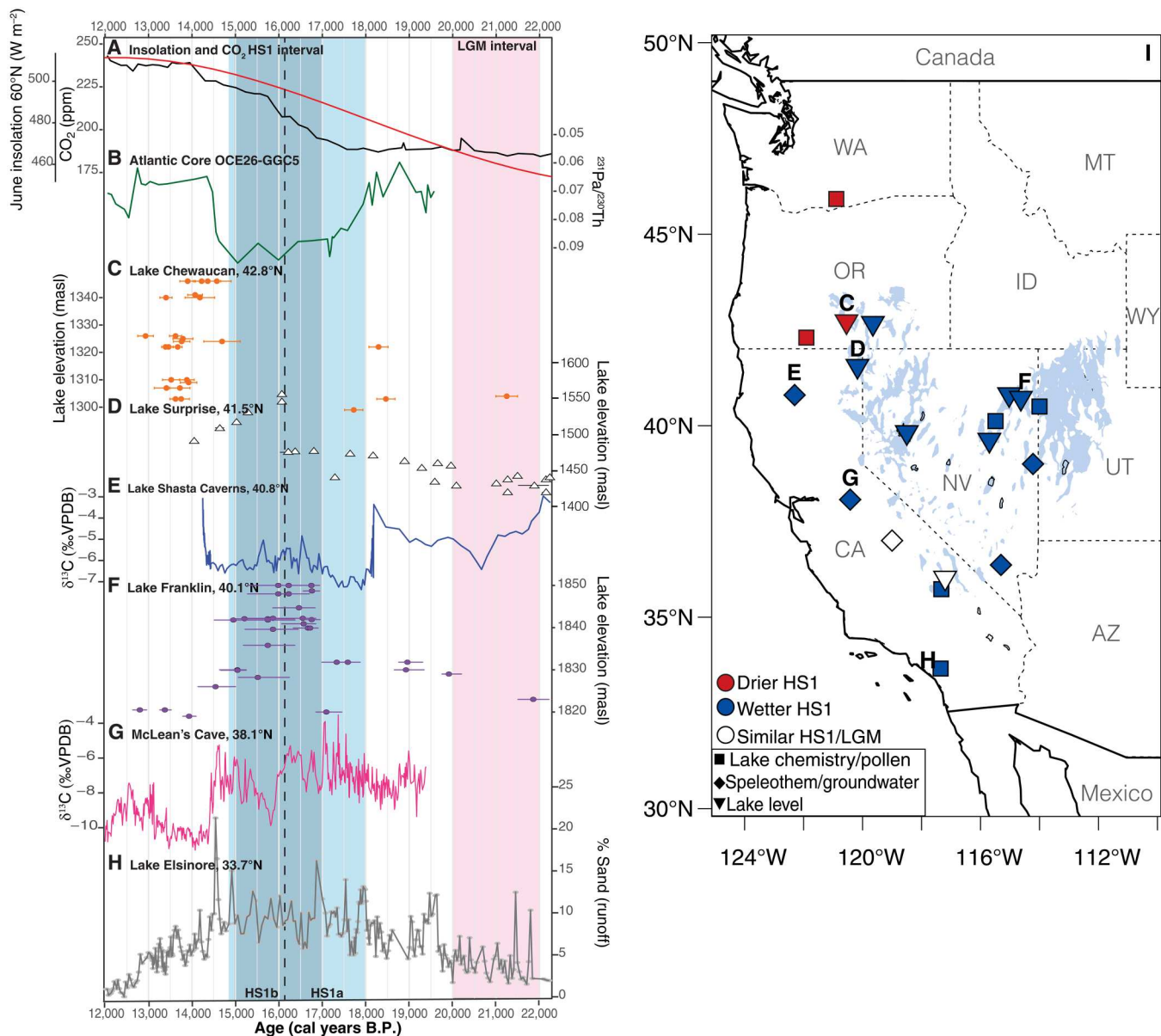
Fig. 1. Summary of climate records for HS1. (**A**) Insolation (*37*) and atmospheric CO_2 [parts per million (ppm)] (*38*). (**B**) Record of $^{231}Pa/^{230}Th$ in the North Atlantic sediment core GGC5, a proxy for AMOC strength (*22*) where strong AMOC is upward on the graph. (**C**) ^{14}C ages and elevation in meters above sea level (masl) for Lake Chewaucan shorelines (*14*). (**D**) ^{14}C ages and elevation in masl for Lake Surprise shorelines (*34*). (**E**) Stable carbon isotopes in the Lake Shasta Caverns Stalagmite in per mil relative to the Vienna Pee Dee Belemnite (‰ VPDB) , a proxy for wetness where a downward shift is wetter conditions (*27*). (**F**) ^{14}C ages and elevation in masl for Lake Franklin shorelines (*15, 71*). (**G**) Stable carbon isotopes in the McLean's Cave stalagmite (ML1) in ‰ VPDB (*24*). (**H**) Percent sand record of runoff from Lake Elsinore sediments where an upward shift is increased runoff (*29*). Pink band indicates time over which LGM conditions are determined for proxies. LGM conditions for ML1 (G) estimated from late glacial record (18,400 to 19,400 years B.P.). Blue band shows entirety of HS1 with gray band indicating interval over which HS1 conditions are determined for comparison to the model time slice (see Materials and Methods). (**I**) Map showing all records used in compilation (see data S1). Blue shading indicates the presence of Great Basin pluvial lakes during this interval. US state abbreviations are as follows: Washington (WA), Oregon (OR), Idaho (ID), Montana (MT), California (CA), Nevada (NV), Utah (UT), Wyoming (WY), and Arizona (AZ). Records shown in time series compilation are demarcated by the corresponding letters.

To understand the driving mechanisms behind the hydroclimate change in western North America during HS1 and to assess the role of ARs and subtropical moisture transport, we use the Community Earth System Model version 1.3 (iCESM1.3) (*20*) to conduct simulations of the LGM climate centered on 21,000 years B.P. [21 thousand years (ka)] as well as several experiments of HS1 climate centered at 16,000 years B.P. (16 ka) to test the sensitivity to freshwater forcing, ice sheets (fig. S1), and sea surface temperatures (SSTs) (Table 1). Our simulations have interactive atmosphere and land components at 0.9° × 1.25° horizontal resolution with prescribed SSTs (fig. S2) from coupled simulations extended from the isotope-enabled transient climate experiment (iTraCE), which

Table 1. 16ka sensitivity experiments. Experiments are performed using CESM1.3 including interactive atmosphere and land components and prescribed SSTs from coupled simulations extended from iTraCE and iTraCE restarts. GHG, greenhouse gas.

Name	Setup
16ka	16-ka orbit, ice sheets, GHG, and prescribed SSTs that do not include freshwater flux
16ka_FWF	16-ka orbit, ice sheets, GHG, and prescribed SSTs that do include freshwater flux
16ka_LGMsst	16-ka orbit, ice sheets, and GHG with LGM SSTs
16ka_LGMice	16-ka orbit, GHG with LGM topography and land surface types, and prescribed SSTs that do not include freshwater flux

simulates robust precipitation increases in the Great Basin around 16 ka (19). The meltwater fluxes in iTraCE were derived from sea level reconstructions and geological markers of ice sheet retreat and meltwater release and primarily represent ice melt into the North Atlantic (20, 21). With the inclusion of meltwater flux, the iTraCE simulation displays a slowdown in Atlantic Meridional Overturning Circulation (AMOC) centered on 16 ka that closely follows that suggested by North Atlantic marine sediment records (Fig. 1B) (20, 22), indicating that a model time slice centered on 16 ka is an appropriate interval to investigate the influence of freshwater flux on HS1 climate. We use several analytical techniques to interpret hydroclimatic change in western North America during these intervals, including water "tagging," which we use to track water from evaporation to precipitation from several regions of the North Pacific, and an AR detection algorithm designed for paleoclimate studies [based on that of (7, 23)]. We compare our model results to a compilation of moisture sensitive proxy records that span the LGM and HS1 intervals in the winter precipitation-dominated region of the western US to assess model agreement with the inferred pattern of hydroclimatic change across the early part of the most recent deglaciation. Our results illustrate the teleconnections between freshwater forcing in the North Atlantic and western North American hydroclimate and highlight the importance of ARs to increasing precipitation in this region during intervals of abrupt global climate change.

RESULTS

HS1 proxy records

Moisture-sensitive proxy records from western North America strongly suggest that the climate of HS1 was wetter than the LGM in the southwestern US and that this wetness extended eastward through the Great Basin. Wetness in western North America is particularly pronounced during the latter part of HS1, sometimes described as HS1b (16,100 to 14,600 years B.P.) (14). As noted in previous data compilations, many Great Basin lakes reached highstands during HS1 (8, 14, 15), and this is evident in our compilation as records throughout the Great Basin indicate a wetter HS1 relative to the LGM (Fig. 1). Several proxy records from California also point to a wetter HS1, including multiproxy stalagmite records from the Sierra Nevada in eastern California (24–26) and the Klamath Mountains in Northern California (27), as well as salinity

proxies from Searle's Lake in the Mojave Desert (28) and sediment proxies of runoff from Lake Elsinore in southern California (29). In contrast, there is no discernable difference between LGM and HS1 lake levels in Panamint Valley (30), and soil opal uranium isotopes from Fish Lake Valley, Nevada, also do not show a clearly wetter HS1 (31). Further north, lake records from Oregon (14, 32) and Washington (33) indicate that the HS1 climate was drier than the LGM. Quantitative estimates of precipitation or effective moisture anomalies between HS1 and the LGM are rare. However, a water balance model based on lake level reconstructions from Lake Surprise in northeastern California suggests that HS1 precipitation was higher than the LGM by ~370 mm/year or ~1 mm/day (34).

Precipitation and low-level winds

The west coast of the US is largely dominated by winter precipitation (17), and winter (DJF) precipitation in the region is higher for all our 16ka iCESM experiments relative to the LGM (21 ka). In the baseline 16ka experiment, the positive winter precipitation anomaly is strongest along the northwestern US coast but extends southward to central California and eastward into the northern Great Basin (Fig. 2C). In 16ka_LGMice, this anomaly is strongest in central California and extends further south (fig. S3). Thus, the main effect of the inclusion of LGM ice sheet topography with 16-ka CO_2 and orbital forcing in this region is a southward shift of the positive precipitation anomaly. The 16ka_LGMsst experiment produces winter precipitation anomalies that are broadly similar to the baseline experiment, but the positive precipitation anomaly is not consistently expressed east of California (fig. S3), indicating that this winter rainfall does not reach as far inland as during the colder LGM. Relative to the LGM simulation, annually averaged precipitation increases along the west coast of the US are either modest and/or not statistically significant for all 16ka experiments apart from the experiment that includes a freshwater flux to the North Atlantic (16ka_FWF) (figs. S4 and S5). By far the most pronounced western US precipitation anomalies relative to the LGM occur when including freshwater forcing to the North Atlantic. The 16ka_FWF experiments display strong positive DJF (Fig. 2, B and D) and annual (fig. S4) precipitation anomalies along the California coast, extending northward into Oregon and Washington and into the northeastern North Pacific. Comparing the 16ka_FWF scenario (Fig. 2, B and D) to the baseline 16ka scenario (Fig. 2, A and C), which only differ by the inclusion of freshwater flux, it is clear that freshwater flux to the North Atlantic expands the positive winter rainfall anomaly over the western coast toward the south and east, extending through California and into the Great Basin, and causes marginally drier conditions along the coast of Washington state (Fig. 2E and fig. S6). CESM is known to have a moderate double ITCZ bias (35), and Dong et al. (36) identify a relationship between the amount of double ITCZ bias in model simulations and future hydroclimate response in the southwest US. However, the potential amount of precipitation response due to double ITCZ bias identified by Dong et al. (36) is smaller than the precipitation response to meltwater flux at 16 ka in our simulations. Therefore, although a double ITCZ bias could contribute to the southwest US precipitation response at 16 ka, it does not change our interpretations. Global winter precipitation in the 16ka, 16ka_FWF, and LGM simulations is shown in fig. S7.

The strong positive precipitation anomaly that develops in the 16ka_FWF scenario relative to the LGM is accompanied by

southwesterly wind anomalies, especially during DJF (Fig. 2). These wind anomalies are also present in the other 16ka experiments during the winter but are considerably weaker, occur only over the central Northern Pacific, and do not extend to the west coast of North America (Fig. 2 and fig. S3). Given the subtle changes induced by the inclusion of the LGM ice sheet and SSTs compared to the larger precipitation and wind anomalies produced by North Atlantic freshwater forcing, we focus below only on the anomalies between the baseline 16ka and 16ka_FWF experiments with the LGM.

Moisture tracking

Through moisture tagging in iCESM1.3, we track changes in the amounts of precipitation at the North American west coast arising from four regions in the North Pacific (Fig. 3 and fig. S8). During the winter (DJF), there is an increase in moisture sourced from the central and subtropical North Pacific for both 16ka simulations with and without freshwater flux relative to the LGM. Increases in precipitation sourced from the central midlatitude North Pacific (CMNP) and central-east North Pacific (CENP) are largest in Washington and Oregon for the baseline 16ka relative to the LGM. In the 16ka_FWF simulation, precipitation from these regions is more abundant, and the anomaly is centered further southward along the California coast and inland toward the Sierra Nevada in eastern California. The 16ka_FWF simulation also sees a larger increase in south-central North Pacific (SCNP) and southeastern North Pacific (SENP) moisture reaching the west coast of the US as compared to the 16ka simulation without freshwater flux.

Atmospheric rivers

The model simulations suggest that precipitation and integrated vapor transport (IVT)—associated with ARs in the North Pacific region—increased at 16 ka relative to the LGM (Fig. 4). Similar to total precipitation, the most pronounced AR precipitation anomalies in the 16ka simulations relative to the LGM occur when North Atlantic freshwater forcing is included. In both the baseline 16ka and 16ka_FWF scenarios, higher AR activity over the ocean is primarily attributable to increased AR frequency and intensity, whereas the frequency, duration, and intensity of ARs behave differently over land between these two simulations. In the baseline 16ka simulation, positive AR precipitation anomalies (up to ~0.5 mm/day) are concentrated over the northwest US region relative to the LGM. Higher AR activity in this region is primarily driven by increased AR intensity (fig. S9) and duration (fig. S10). With the addition of freshwater forcing in the North Atlantic, AR precipitation anomalies are further enhanced (up to 3 mm/day) and expand southward and further inland along the west coast of the US (Fig. 4). In the 16ka_FWF scenario, increased AR precipitation is primarily driven by more frequent AR events closer to the coast (fig. S11) and longer AR events in the Great Basin (fig. S10). The average number of ARs increases by ~2 and 8 events per year at coastal proxy sites in the 16ka and 16ka_FWF simulations, respectively, relative to the LGM (fig. S12). In addition, ARs comprise a larger portion of total wintertime precipitation at 16 ka relative to the LGM (fig. S13).
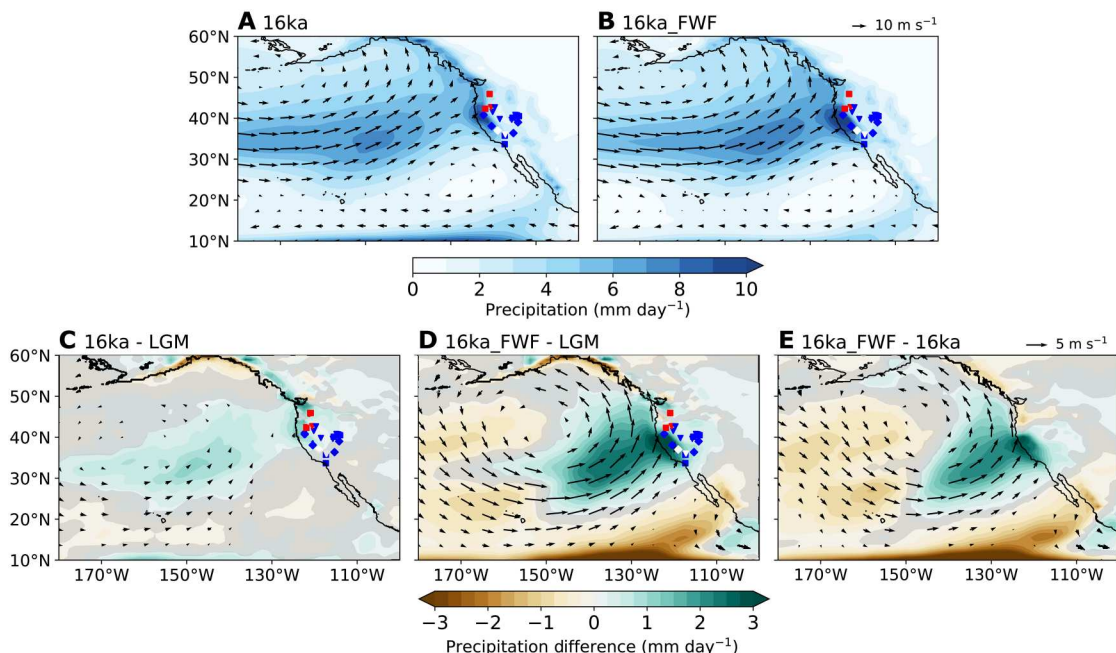
Fig. 2. Winter (DJF) precipitation and 850hPa (horizontal) winds and anomalies. - Results for (**A**) 16ka and (**B**) 16ka_FWF simulations. Winter precipitation and 850-hPa wind anomalies for the (**C**) 16ka and (**D**) 16ka_FWF simulations relative to the LGM, respectively, and (**E**) 16ka_FWF relative to the baseline 16ka simulation. Differences in precipitation and winds that are not significant at the 95% level ($P > 0.05$ using a Student's t test) are shaded with gray and omitted from the plot, respectively. Winds at 850 hPa over land do not change substantially and thus have been omitted for plotting purposes. Western US hydroclimatic proxy records are the same as in Fig. 1.
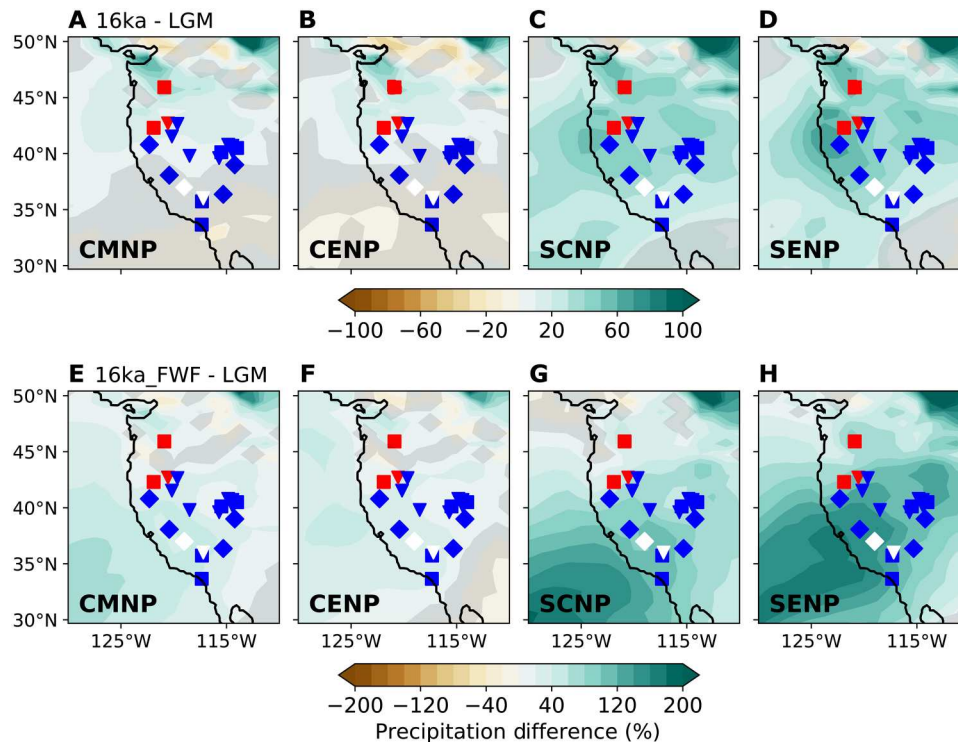
Fig. 3. Water tagging results. Wintertime (DJF) precipitation from tagged water in the baseline 16ka simulation in (**A**) CMNP (20°N to 45°N, 140°W to 180°W), (**B**) CENP (20°N to 45°N, 110°W to 140°W), (**C**) SCNP (10°N to 20°N,140°W to 180°W), and (**D**) SENP (10°N to 20°N, 100°W to 140°W) relative to the LGM simulation. (**E** to **H**) The same tagging results are also plotted for the 16ka_FWF simulation. Western US hydroclimatic proxy records are the same as in Fig. 1. Areas from which moisture is tracked and tracking results for the northeastern Pacific are shown in fig. S8. Differences in precipitation that are not significant at the 95% level (*P* > 0.05 using a Student's *t* test) are shaded with gray.

DISCUSSION

For all our experiments, positive annual and winter precipitation anomalies are present in parts of western North America for 16 ka relative to the LGM. The increased wetness in the Pacific Northwest in the baseline 16ka simulation relative to the LGM likely arises due to orbital changes and increases in atmospheric CO_2 [see Materials and Methods, (*37*, *38*), and Fig. 1A] that drive a warmer and wetter climate. Relative to the LGM, stronger westerly winds in the North Pacific and a deeper Aleutian low lead to increased Central Pacific moisture reaching the west coast at 16 ka (Fig. 3), even when freshwater forcing is not included.

The inclusion of freshwater flux to the North Atlantic has the largest influence on winter precipitation in western North America relative to the baseline 16ka simulation and other sensitivity experiments. Compared to the baseline 16ka scenario, the winter (Fig. 2) and annual (figs. S4 and S6) precipitation anomalies are shifted equatorward and extend farther eastward (Fig. 2E) with the inclusion of freshwater forcing. To compare the spatial patterns of winter precipitation anomalies between the baseline 16ka and 16ka_FWF scenarios relative to the LGM with paleoclimate observations from this region, we computed the Gwet's agreement coefficient (AC) (*39*) between the simulated anomalies and the proxy compilation (see Materials and Methods). We use Gwet's AC to evaluate categorical agreement between proxies and models, which independently assess whether each proxy locality experienced wetter, drier, or unchanged conditions at 16 ka relative to the LGM (*39*). We evaluate agreement between the proxy

compilation and the model scenarios relative to random chance agreement across a range of threshold values (5 to 20%) for which a change in precipitation observed by the models would be considered wetter or drier (see Materials and Methods). The baseline 16ka simulation has a maximum AC value of 0.69 at a low precipitation anomaly threshold of 5% (Fig. 5). The AC value decreases quickly as the threshold is raised and a larger precipitation anomaly is required to categorize a site as wetter or drier in the model (fig. S14). The 16ka_FWF simulation has a maximum AC value of 0.78 at a precipitation threshold of 19% (Fig. 5). However, AC values are high, and above 0.71, at thresholds of 5 to 19%, suggesting that this higher AC value with freshwater flux is robust regardless of the threshold chosen (fig. S14). The 16ka_FWF simulation likely has a higher AC value because the positive precipitation anomaly stretches farther to the south. In addition, although the freshwater flux scenario does not indicate reduced precipitation at the exact proxy locations in the northwestern US, drier conditions, nevertheless, prevail in the region between these proxy data sites (Fig. 5). Thus, the inclusion of freshwater flux to the North Atlantic leads to a noticeable improvement in model-proxy agreement in the western US when comparing differences between the HS1 and LGM climates. For a quantitative comparison, at Lake Surprise in northeastern California, the freshwater flux scenario leads to a positive precipitation anomaly (0.36 mm/day, annual; 0.72 mm/day, DJF) that is close to that estimated by Ibarra *et al.* (*34*) on the basis of lake water balance calculations (~1 mm/day) and higher than anomalies in the baseline 16ka scenario.
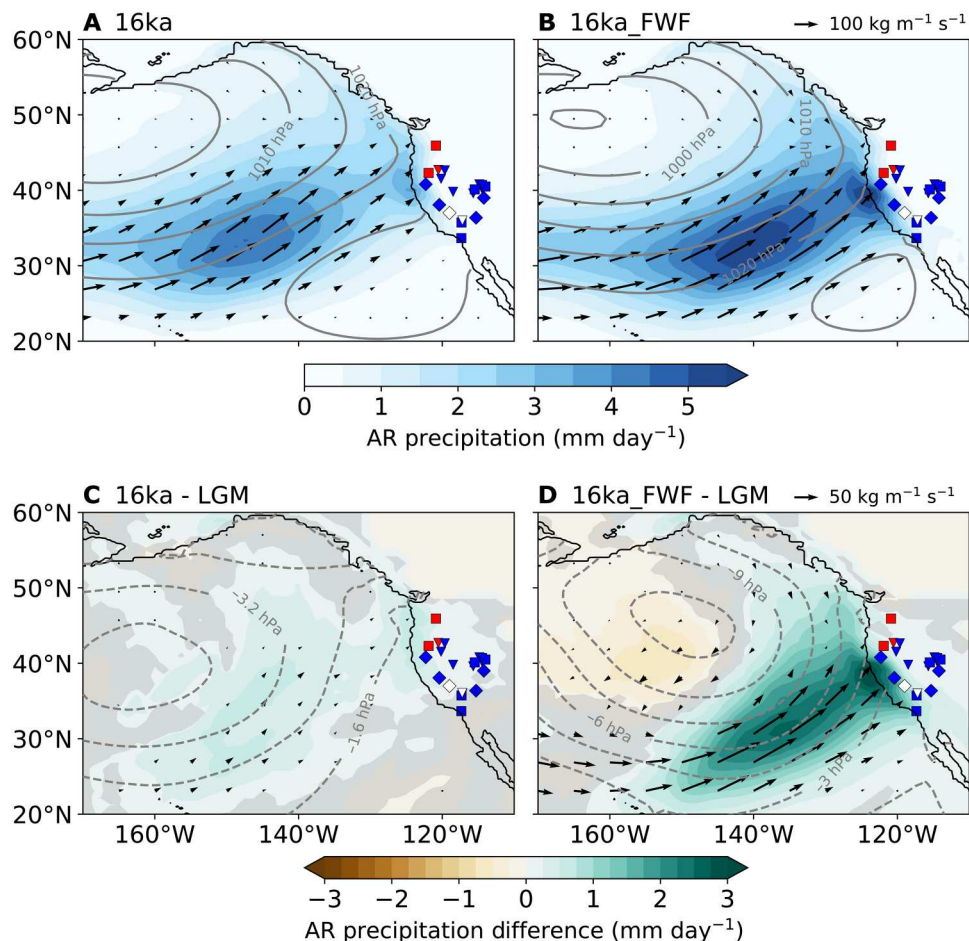
Fig. 4. Winter (DJF) precipitation, sea level pressure, and IVT associated with ARs. (**A**) 16ka and (**B**) 16ka_FWF. Differences in AR precipitation, sea level pressure, and integrated vapor transport (IVT) for the (**C**) 16ka and (**D**) 16ka_FWF simulations relative to the LGM. Note that contours of sea level pressure differences are plotted in increments of 0.3 and 1.5 hPa in (C) and (D), respectively. Differences in precipitation and winds that are not significant at the 95% level ($P > 0.05$ using a Student's t test) are shaded with gray, and insignificant differences in winds are omitted from the plot, respectively. IVT and sea level pressure over land are removed for plotting purposes. Western US hydroclimatic proxy records are the same as in Fig. 1.

In a set of idealized LGM experiments with North Atlantic freshwater forcing, McGee *et al.* (*8*) attributed increased winter precipitation in western North America to an intensification of the east-central Pacific Hadley circulation and increased moisture transport by ARs. In our simulations that include more realistic boundary conditions for HS1 (including 16-ka orbital forcing, greenhouse gases, and ice sheets), water tagging indicates that the increased precipitation along the US west coast is predominantly coming from the central North Pacific. The inclusion of North Atlantic freshwater forcing leads to increased precipitation sourced from the central North Pacific, SCNP, and SENP (Fig. 3 and fig. S8) relative to the LGM and to the baseline 16ka simulation.

Similar to the interpretation outlined schematically in figure 5 of (*8*), we find that the ascending branch of the Hadley circulation is shifted into the Southern Hemisphere (i.e., the summer hemisphere) in the 16ka_FWF simulation relative to the baseline 16ka simulation. This latitudinal shift yields a local Rossby wave source (*40*) in the eastern tropical Pacific that excites northward propagating Rossby waves that help strengthen the Aleutian Low and create favorable conditions for moisture transport into the southwestern

US (Fig. 6B). The wave response in the deep tropics is, to first-order, comparable to that observed by Sardeshmukh and Hoskins (*40*), who investigated the wave response to upper tropospheric divergence in the deep tropics in an idealized, linear circulation model. This apparent similarity between studies suggests that the interpretation by McGee *et al.* (*8*) of an intensification of the east-central Pacific Hadley circulation is both plausible and, at least, a partial explanation for the changes in the stationary wave field.

McGee *et al.* (*8*), however, solely invoke tropical-extratropical connections and do not account for the extratropical wave interactions that have been identified elsewhere. For example, previous work has shown that the strong zonal wind in glacial climates acts as a wave guide for stationary waves, resulting in complex wave patterns that are controlled by the superposition of reflecting and refracting waves in extratropical latitudes (*9, 41, 42*). The picture that emerges in our simulations suggests that these extratropical wave interactions are also occurring in the 16ka_FWF scenario (Fig. 6). Therefore, the full-wave response to freshwater forcing should perhaps best be viewed as a combination of both tropical and
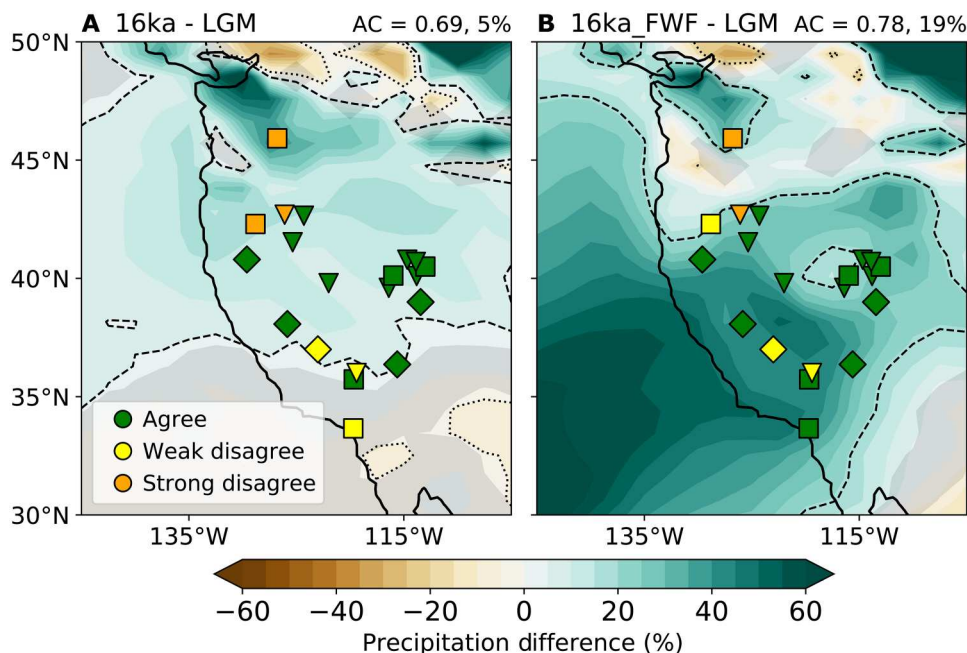
Fig. 5. Proxy-model agreement. Agreement between proxy compilation and the baseline 16ka scenario (**A**) and 16ka_FWF scenario (**B**) with their maximum computed AC. Winter (DJF) precipitation anomalies between the 16ka scenarios and the LGM are plotted as percent anomalies. Differences in precipitation that are not significant at the 95% level (*P* > 0.05 using a Student's *t* test) are shaded with gray. Dashed lines indicate the threshold of precipitation change at which the maximum AC value is found (thick dashed line, positive precipitation change threshold; thin dashed line, negative precipitation change threshold). Proxy symbols are color-coded by how well they agree with the models at each location.

extratropical wave sources and interactions, rather than the response to waves originating in either region in isolation.

Our analysis offers insights into the importance of freshwater forcing and the associated SST cooling in the North Atlantic for generating increased winter wetness in western North America through increases in moisture flux from the Central and subtropical Pacific, particularly through an increase in the influence of AR events affecting the west coast. Limitations of our study stem from the chronologic uncertainty and potential unaccounted for seasonal bias of proxy records that can complicate systematic comparisons between proxies and seasonal model output. To mitigate these limitations, we restrict our study area to the portion of the western US where the annual balance of precipitation is strongly dominated by winter rain and snowfall (*17*), and, thus, proxies should predominantly reflect changes in winter precipitation. We also choose records that include robust chronologic constraints in both the late glacial/LGM and HS1 intervals. Furthermore, the increase in ARs reaching western North America observed in the model with the inclusion of freshwater forcing supports previous interpretations of individual proxy records. For example, at McLean's Cave in central California, west of the Sierra Nevada, the amount of winter AR precipitation increases from 0.5 mm/day in the LGM simulation to 0.73 mm/day for the baseline 16ka experiment and to 2.06 mm/day for the 16ka_FWF simulation (Fig. 4 and data S1). For the 16ka_FWF simulation, the proportion of AR precipitation out of total DJF precipitation increases from ~7 to 20% (fig. S13), and the average number of AR events per year increases from ~2 to 8 relative to the LGM (fig. S12). This finding is consistent with the McLean's Cave proxy records that suggest both a wetter climate during HS1, as indicated by a shift to lower values in the

calcite stable carbon isotope record (Fig. 1G) and inclusion fluid hydrogen and oxygen isotope records, and an increase in moisture from warm, wet storms from the subtropical Pacific, as indicated by a positive shift in the calcite stable oxygen isotope record during HS1 relative to the late glacial (*23–26*). Shifts in speleothem carbon and oxygen isotope records between the LGM and HS1 are evident further north at Lake Shasta Caverns, California (Fig. 1E) (*27*) and are also consistent with our modeled increase in AR storms in the 16ka_FWF simulation. Similar increases in precipitation and storminess have been suggested on the northern and central California coast by speleothem and lake sediment proxy records of the 8.2-ka event, another interval characterized by enhanced freshwater flux to the North Atlantic (*43*, *44*).

Increases in AR precipitation have been postulated to have supported the rise of Great Basin pluvial lakes to their post-LGM highstands (*8*). Our results indicate that AR precipitation contributes most to enhanced winter precipitation along the west coast, with impacts centered on California. However, modest increases in AR precipitation do occur in the eastern Great Basin, where lakes reached highstands between 16 and 17 ka. ARs contribute almost no winter precipitation in the LGM simulation (0 to 0.2 mm/day) in the areas of Lakes Bonneville, Franklin, Clover, and Waring, but, in the 16ka_FWF scenario, these areas see up to ~2 ARs per year (fig. S12) that contribute ~0.1 mm/day on average over the winter (data S1). The increases in AR precipitation in both HS1 scenarios are even greater in the western Great Basin where pluvial lakes reach their post glacial highstands slightly later in the deglaciation (*8*, *14*). At Lakes Lahontan and Surprise, both of which see highstands close to 16 ka (*14*, *34*), AR precipitation increases by two to four ARs per year in the 16ka_FWF simulation relative to the LGM (fig. S12). At
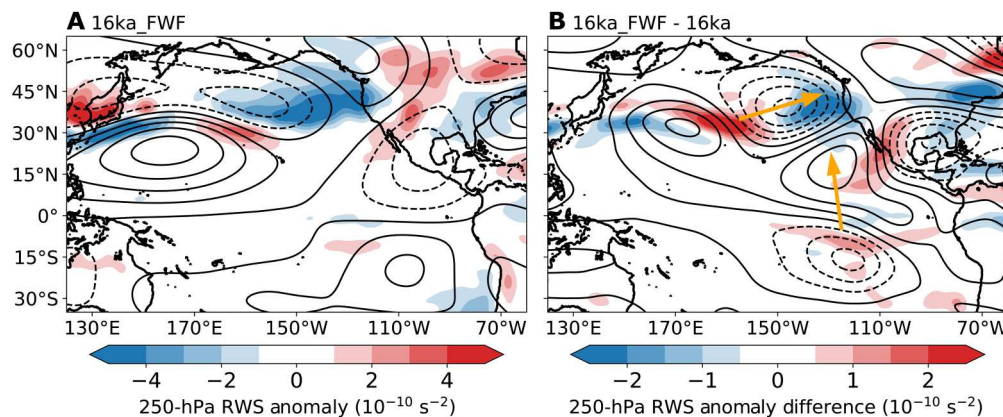
Fig. 6. Atmospheric dynamics. Winter (DJF) eddy stream function (contours; geostrophic stream function with the zonal mean removed) and Rossby wave source at 250 hPa (shading) in the (**A**) 16ka_FWF simulation and (**B**) 16ka_FWF relative to the 16ka simulation. Orange arrows indicate the approximate direction of wave propagation. Solid and dashed contours indicate positive and negative values of eddy stream function, respectively. Black contours in (A) and (B) are plotted at 0.65 and 0.25 (m^2 s^{-1} × 10^7) increments, respectively.

Lake Chewaucan, where the highstand is dated to ~14 ka during the Bølling Allerød, our simulations indicate a similar increase in AR precipitation. Although dated tufa deposits indicate a relatively high lake during the LGM, there is no dated shoreline material for Lake Chewaucan during HS1 (Fig. 1C), which has been interpreted to reflect lake regression during this time (*14*). Both the baseline 16ka and 16ka_FWF scenarios suggest wetter conditions at this site relative to the LGM (Figs. 2 and 5 and fig. S4), indicating that these anomalies may extend too far north in our model scenarios or that wet or rising conditions at the lake were not recorded by shoreline deposits during this interval. Thus, another limitation of our study stems from our imposed ice sheet reconstruction that may contribute to precipitation biases in the model in the northern part of our study area where regional ice sheet geometry likely played an important role in the hydroclimate response. In addition, our simulations are run at 0.9° × 1.25° horizontal resolution and thus do not fully capture the fine-scale dynamic and thermodynamic processes that shape AR intensity or the topographic resolution of western US mountain ranges, limiting our ability to assess orographic precipitation and rain shadow effects (*45*). Future simulations at higher resolution (e.g. 0.23° × 0.31°) may improve model-proxy agreement in this topographically complex region. Furthermore, these simulations do not include land surface responses such as lakes or vegetation change that could have amplified the hydroclimate response further inland at the locations of the eastern Great Basin Lakes. The inclusion of these feedbacks in future simulations as well as the addition of tagging and AR tracking to model simulations of later stages in the deglaciation, including the Bølling Allerød (e.g., 15 and 14 ka), may help to resolve spatiotemporal variations in the impacts of AR precipitation on the timing of pluvial lake highstands in western North America.

In these simulations, freshwater forcing, primarily into the North Atlantic, and associated North Atlantic cooling result in increased winter precipitation derived from the eastern North Pacific as well as increased frequency and duration of AR storms along the west coast of the US. Freshwater forcing during HS1 is linked to a slowdown of AMOC in both models and proxies (*20*), although recent proxy compilations suggest that AMOC may have been only 30% slower in HS1 compared to the LGM (*46*). Marine sediment records indicate that melting of European ice sheets initiated a slowdown of AMOC early in HS1, which was subsequently amplified by release of icebergs from the Laurentide Ice Sheet during the latter part of HS1 (*47–49*). Recent indicators of AMOC strength point to an unprecedented decline in the 20th century leaving AMOC in its weakest state in the past 1000 years (*50–52*). Model experiments using an earlier version of the atmospheric model (Community Atmosphere Model version 4) found similar patterns of increased precipitation across the Pacific that is suggestive of increased ARs in response to an AMOC shutdown with global warming, although the increase in western US precipitation was not statistically significant (*53*, *54*). Overall, our results point to a clear connection between conditions in the North Atlantic and AR activity in the northeastern Pacific that may have important implications for hydroclimate and resource planning under an anthropogenically modified climate.

MATERIALS AND METHODS
Experimental design
Here, we use the iCESM1.3 (*20*). The climate of CESM1.3 is broadly similar to CESM1.2, which captures the observed preindustrial and historical mean state and variability to a high accuracy (*55*). The atmospheric component of iCESM1.3 is the Community Atmosphere Model version 5 (*56*, *57*), and the land model is version 4 of the Community Land Model (*58*). The simulations presented here have interactive atmosphere and land components at 0.9° × 1.25° horizontal resolution. Prescribed SSTs come from coupled simulations extended from iTraCE (see below). All analyses use the final 45 years of model outputs.

Our LGM boundary conditions follow the Paleoclimate Modelling Intercomparison Project protocols (*59*), including ICE-6G ice sheet reconstructions (*60*) (fig. S1), 21-ka orbital configurations (*37*) and 190–parts per million (ppm) CO$_2$ (*38*). A description of our LGM simulation can also be found in (*13*). Our HS1 boundary conditions include 16-ka ice reconstruction from ICE-6G, 224-ppm CO$_2$ (*38*), and 16-ka orbital configuration (*37*). We use prescribed SSTs from the iTraCE simulation for our 16ka_FWF simulation and from simulations branched from iTraCE restarts that do not include

freshwater flux for the other sensitivity experiments (fig. S2). Freshwater flux in the iTraCE simulation (20) mimics the scheme used in the TraCE-21ka simulations (21). In the iTraCE simulation, most freshwater flux before 16 ka is released into the surface ocean of the North Atlantic (80°W to 20°E/50°N to 70°N). Before 17 ka, a secondary amount of freshwater is added to the Gulf of Mexico (255°E to 280°E/15°N to 33°N), but it has little impact on climate relative to the North Atlantic freshwater flux, especially by 16 ka (21). In the iTraCE simulation that includes freshwater flux, a slowdown in AMOC of ~12 sverdrups (Sv) occurs from 17.5 to 15.5 ka as meltwater flux to the North Atlantic is increased. This closely follows the $^{231}Pa/^{230}Th$ marine sediment proxy of AMOC intensity (20, 22).

We use several analysis techniques to interpret hydrologic change in the western US at the LGM and HS1. To better understand the sources of moisture reaching the western US, we use the water tagging feature within iCESM1.3, which tracks water from evaporation to deposition in user defined regions. Water tags are passive and do not influence the simulated climate. Here, we focus on regions within the North Pacific, as this area is the source of the vast majority of moisture transported to the western US. We track moisture originating from four regions (Fig. 3): the CMNP (here defined as the region 20°N to 45°N, 180°W to 140°W), CENP (20°N to 45°N, 110°W to 140°W), SCNP (10°N to 20°N, 180°W to 140°W), and SENP (10°N to 20°N, 100°W to 140°W).

ARs are identified in the North Pacific and SWNA regions using an automated tracking method that has previously been used in paleoclimate studies (7, 23, 61–63). We define ARs as contiguous regions of at least 2000 km where 6-hourly (instantaneous) vertically IVT exceeds a threshold value. The magnitude of IVT is calculated as

$$IVT = \left[\left(\frac{1}{g} \int_{p_s}^{0} qudp \right)^2 + \left(\frac{1}{g} \int_{p_s}^{0} qvdp \right)^2 \right]^{\frac{1}{2}}$$

where g is the gravitational acceleration, p_s is surface pressure, q is specific humidity, u is zonal wind, v is meridional wind, and the integral is carried out over pressure p from the surface to the top of the atmosphere. The threshold value of IVT is based on zonal-mean integrated water vapor (IWV), and ARs are detected when

$$IVT \geq IVT_{min} \left(1 - \frac{IWV}{\max(\overline{IWV})} \right)^{-1}$$

where IWV is the 30-day running mean of the zonally averaged IWV, $\max(\overline{IWV})$ is the latitudinal maximum of IWV, and IVT_{min} is equal to 225 kg/m/s. The algorithm incorporates aspects of both absolute threshold-based (IVT_{min}) and relative (use of background IWV) AR tracking methodologies (64, 65). Compared to the median of all tracking methods included in the Atmospheric River Tracking Method Intercomparison Project, this algorithm detects the same month of peak AR frequency and a higher magnitude and range of AR frequency in the western US (65). Nevertheless, this algorithm allows for comparison between climates with different mean states and thus is well suited for comparing ARs across multiple paleoclimate intervals.

Following (23, 60), AR frequencies are calculated as the percentage of 6-hourly time steps in which an AR is detected divided by the total number of 6-hourly time steps in the specified analysis period.

Following (63), AR durations are calculated as the continuous length of time that a given location is experiencing AR conditions (i.e., is located within the spatial extent of an AR defined by the AR tracking method). AR intensity is inferred from the average IVT of AR conditions at a given location. Precipitation from ARs is calculated on the basis of the colocation of precipitation and identified ARs, where precipitation occurring where AR conditions are met is counted as AR precipitation. This definition of AR precipitation includes tropical moisture intrusion and frontal systems that meet the same criteria of length and IVT.

Proxy compilation
We compiled paleoclimate proxy records from the western US that cover both the LGM (21,000 ± 1000 years) and HS1. We focused on the region of the western US where the annual balance of precipitation is dominated by winter rain and snowfall (17). Thus, our compilation covers the region between the Mexican and Canadian borders, stretches from the west coast eastward through the Great Basin to 114° W. In the western US, it has been suggested that HS1 can be divided into two intervals with distinct regional hydroclimate: HS1a that covers 18.0 to 16.1 ka and HS1b that covers 16.1 to 14.6 ka (14). For our comparison, we noted the moisture designation for HS1 proxy records as they covered 16,000 years B.P. ± 1000 years (Fig. 1). This interval aligns with the slowdown of AMOC observed in $^{231}Pa/^{230}Th$ from North Atlantic sediments (Fig. 1B) (22) and overlaps mostly with HS1b that is the more consistently wet interval of HS1 (14, 26). Thus, if the authors specifically noted a proxy response during HS1b, which has also been called "The Big Wet" (66), then we used this proxy designation in our compilation. Our proxy interpretations are based on those of the original authors of each study. We assigned a proxy response of "w" if the record suggests a wetter climate during HS1 relative to the LGM; "d" if the proxy suggests a drier climate during HS1 relative to the LGM; and "n" if HS1 and the LGM are too similar to be distinguished in the proxy record. LGM conditions are determined for 21,000 ± 1000 years B.P. for each record with the exception of the ML1 stalagmite (24–26), which extends to 19,400 years B.P. For this record, we take the late glacial portion of the carbon isotope record (18,400 to 19,400 years B.P.) to represent LGM climate at this site. Records included in our proxy compilation are provided in data S1.

Statistical analysis
We conduct a proxy-model comparison between the results of our baseline 16ka and 16ka_FWF scenarios and proxy compilation using the Gwet's AC statistic. Gwet's AC evaluates categorical agreement between two raters (proxies and models) that classify items (sites) into categories (wetter, drier, and no change) relative to the probability of random chance agreement (39, 67–69). The AC statistic is given by

$$AC = \frac{P_a - P_e}{100\% - P_e}$$

where P_a is the percentage of agreement between the proxies and the model output and P_e is the expected percentage of agreement between the two due to chance. If models and proxies are in complete agreement, then AC = 1. If there is no agreement beyond what is expected from random chance, then AC = 0. The Gwet's AC

statistic weights observations based on the degree of model-proxy agreement by multiplying a matrix of the model-proxy observations by a weight matrix in which a strong agreement (e.g., both model and proxy indicate that a site is "wetter" or "drier") is given a weight of 1, a strong disagreement (e.g., the model or proxy indicates that a site is drier and the other indicates that a site is wetter) is given a weight of 0, and a weak disagreement (e.g., the model or proxy indicates that a site is wetter or drier and the other indicates that a site has "no change") is given a weight of 0.5. We compute the AC using the modeled DJF precipitation anomalies between the 16ka and LGM model scenarios computed as percent change in precipitation relative to the LGM for the grid cell in which each proxy record is located. To identify maximum possible agreement between the model and proxy compilation, we vary the threshold value for which a change in precipitation would be considered wetter or drier from 5 to 20% in 1% increments. For example, at a threshold of 10%, the model must simulate 16-ka precipitation ≥ 110% of the LGM to be considered wetter and ≤ 90% of the LGM to be considered drier. All precipitation thresholds tested are above the level of significance ($P < 0.05$ using a Student's t test) for winter precipitation anomalies.

Supplementary Materials

This PDF file includes:
Figs. S1 to S14
Legend for data S1

Other Supplementary Material for this manuscript includes the following:
Data S1

REFERENCES AND NOTES

1. Y. Zhu, R. E. Newell, A proposed algorithm for moisture fluxes from atmospheric rivers. *Mon. Weather Rev.* **126**, 725–735 (1998).
2. A. E. Payne, M.-E. Demory, L. R. Leung, A. M. Ramos, C. A. Shields, J. J. Rutz, N. Siler, G. Villarini, A. Hall, F. M. Ralph, Responses and impacts of atmospheric rivers to climate change. *Nat. Rev. Earth Environ.* **1**, 143–157 (2020).
3. M. D. Dettinger, Atmospheric rivers as drought busters on the U.S. West Coast. *J. Hydrometeorol.* **14**, 1721–1732 (2013).
4. F. M. Ralph, J. J. Rutz, J. M. Cordeira, M. Dettinger, M. Anderson, D. Reynolds, L. J. Schick, C. Smallcomb, A scale to characterize the strength and impacts of atmospheric rivers. *Bull. Am. Met. Soc.* **100**, 269–289 (2019).
5. X. Huang, D. L. Swain, Climate change is increasing the risk of a California megaflood. *Sci. Adv.* **8**, eabq0995 (2022).
6. B. J. Hatchett, D. P. Boyle, C. B. Garner, M. L. Kaplan, A. E. Putnam, S. D. Bassett, Magnitude and frequency of wet years under a megadrought climate in the western Great Basin, USA. *Quat. Sci. Rev.* **152**, 197–202 (2016).
7. J. M. Lora, J. L. Mitchell, C. Risi, A. E. Tripati, North Pacific atmospheric rivers and their influence on western North America at the Last Glacial Maximum. *Geophys. Res. Lett.* **44**, 1051–1059 (2017).
8. D. McGee, E. Moreno-Chamarro, J. Marshall, E. D. Galbraith, Western U.S. lake expansions during Heinrich stadials linked to Pacific Hadley circulation. *Sci. Adv.* **4**, eaav0118 (2018).
9. M. Lofverstrom, A dynamic link between high-intensity precipitation events in southwestern North America and Europe at the Last Glacial Maximum. *Earth Planet. Sci. Lett.* **534**, 116081 (2020).
10. M. C. Reheis, K. D. Adams, C. G. Oviatt, S. N. Bacon, Pluvial lakes in the Great Basin of the western United States—A view from the outcrop. *Quat. Sci. Rev.* **97**, 33–57 (2014).
11. C. Morrill, D. P. Lowry, A. Hoell, Thermodynamic and dynamic causes of pluvial conditions during the Last Glacial Maximum in western North America. *Geophys. Res. Lett.* **45**, 335–345 (2018).
12. J. M. Lora, Components and mechanisms of hydrologic cycle changes over North America at the Last Glacial Maximum. *J. Climate* **31**, 7035–7051 (2018).
13. C. Tabor, M. Lofverstrom, J. Oster, B. Wortham, C. de Wet, I. Montañez, A. Rhoades, C. Zarzycki, C. He, Z. Liu, A mechanistic understanding of oxygen isotopic changes in the Western United States at the Last Glacial Maximum. *Quat. Sci. Rev.* **274**, 107255 (2021).
14. A. M. Hudson, B. J. Hatchett, J. Quade, D. P. Boyle, S. D. Bassett, G. Ali, M. G. De los Santos, North-south dipole in winter hydroclimate in the western United States during the last deglaciation. *Sci. Rep.* **9**, 4826 (2019).
15. J. S. Munroe, B. J. Laabs, Temporal correspondence between pluvial lake highstands in the southwestern US and Heinrich Event 1. *J. Quat. Sci.* **28**, 49–58 (2013).
16. S. R. Hemming, Heinrich events: Massive late Pleistocene detritus layers of the North Atlantic and their global climate imprint. *Rev. Geophys.* **42**, RG1005 (2004).
17. J. M. Lora, D. E. Ibarra, The North American hydrologic cycle through the last deglaciation. *Quat. Sci. Rev.* **226**, 105991 (2019).
18. J. M. Lora, J. L. Mitchell, A. E. Tripati, Abrupt reorganization of North Pacific and western North American climate during the last deglaciation. *Geophys. Res. Lett.* **43**, 11796–11804 (2016).
19. M. Fu, Revisiting western United States hydroclimate during the last deglaciation. *Geophys. Res. Lett.* **50**, e2022GL101997 (2023).
20. C. He, Z. Liu, B. L. Otto-Bliesner, E. C. Brady, C. Zhu, R. Tomas, P. U. Clark, J. Zhu, A. Jahn, S. Gu, J. Zhang, J. Nusbaumer, D. Noone, H. Cheng, Y. Wang, M. Yan, Y. Bao, Hydroclimate footprint of pan-Asian monsoon water isotope during the last deglaciation. *Sci. Adv.* **7**, eabe2611 (2021).
21. F. He, "Simulating transient climate evolution of the last deglaciation with CCSM 3," thesis, University of Wisconsin–Madison, Madison, WI, 2011.
22. J. F. McManus, R. Francois, J.-M. Gherardi, L. D. Keigwin, S. Brown-Leger, Collapse and rapid resumption of Atlantic meridional circulation linked to deglacial climate changes. *Nature* **428**, 834–837 (2004).
23. C. B. Skinner, J. M. Lora, A. E. Payne, C. J. Poulsen, Atmospheric river changes shaped midlatitude hydroclimate since the mid-Holocene. *Earth Planet. Sci. Lett.* **541**, 116293 (2020).
24. J. L. Oster, I. P. Montañez, L. R. Santare, W. D. Sharp, C. Wong, K. M. Cooper, Stalagmite records of hydroclimate in central California during termination 1. *Quat. Sci. Rev.* **127**, 199–214 (2015).
25. B. E. Wortham, I. P. Montañez, D. J. Rowland, M. Lerche, A. Browning, Mapping fluid-filled inclusions in stalagmites using coupled X-ray and neutron computed tomography: Potential as a water excess proxy. *Geochem. Geophys. Geosyst.* **20**, 2647–2656 (2019).
26. B. E. Wortham, I. P. Montañez, P. K. Swart, H. Vonhof, C. Tabor, Variability in effective moisture inferred from inclusion fluid $\delta^{18}O$ and δ^2H values in a central Sierra Nevada stalagmite (CA). *Quat. Sci. Rev.* **279**, 107399 (2022).
27. J. L. Oster, I. E. Weisman, W. D. Sharp, Multi-proxy stalagmite records from northern California reveal dynamic patterns of regional hydroclimate over the last glacial cycle. *Quat. Sci. Rev.* **241**, 106411 (2020).
28. M. D. Peaple, T. Bhattacharya, T. K. Lowenstein, D. McGee, K. J. Olson, J. S. Stroup, J. E. Tierney, S. J. Feakins, Biomarker and pollen evidence for late Pleistocene pluvials in the Mojave Desert. *Paleoceanogr. Paleoclimatol.* **37**, e2022PA004471 (2022).
29. M. E. Kirby, L. Heusser, C. Scholz, R. Ramezan, M. A. Anderson, B. Markle, E. Rhodes, K. C. Glover, J. Fantozzi, C. Hiner, B. Price, H. Rangel, A late Wisconsin (32–10 cal ka BP) history of pluvials, droughts, and vegetation in the Pacific south-west United States (Lake Elsinore, CA). *J. Quat. Sci.* **33**, 238–254 (2018).
30. A. S. Jayko, R. M. Forester, D. S. Kaufman, F. M. Phillips, J. C. Yount, J. McGeehin, S. A. Mahan, Late Pleistocene lakes and wetlands, Panamint Valley, Inyo County, California. *Geol. Soc. Am. Bull.* **439**, 151–184 (2008).
31. K. Maher, D. E. Ibarra, J. L. Oster, D. M. Miller, J. L. Redwine, M. C. Reheis, J. W. Harden, Uranium isotopes in soils as a proxy for past infiltration and precipitation across the western United States. *Am. J. Sci.* **314**, 821–857 (2014).
32. M. A. Worona, C. Whitlock, Late quaternary vegetation and climate history near Little Lake, central Coast Range, Oregon. *Geol. Soc. Am. Bull.* **107**, 867–876 (1995).
33. C. Whitlock, P. J. Bartlein, Vegetation and climate change in northwest America during the past 125 kyr. *Nature* **388**, 57–61 (1997).
34. D. E. Ibarra, A. E. Egger, K. L. Weaver, C. R. Harris, K. Maher, Rise and fall of late Pleistocene pluvial lakes in response to reduced evaporation and precipitation: Evidence from Lake Surprise, California. *Geol. Soc. Am. Bull.* **126**, 1387–1415 (2014).
35. O. Adam, T. Schneider, F. Brient, Regional and seasonal variations of the double-ITCZ bias in CMIP5 models. *Climate Dynam.* **51**, 101–117 (2018).
36. L. Dong, L. R. Leung, J. Lu, F. Song, Double-ITCZ as an emergent constraint for future precipitation over Mediterranean climate regions in the North Hemisphere. *Geophys. Res. Lett.* **48**, e2020GL091569 (2021).
37. J. Laskar, A. Fienga, M. Gastineau, H. Manche, La2010: A new orbital solution for the long-term motion of the Earth. *Astron. Astrophys.* **532**, A89 (2011).

38. D. Lüthi, M. Le Floch, B. Bereiter, T. Blunier, J.-M. Barnola, U. Siegenthaler, D. Raynaud, J. Jouzel, H. Fischer, K. Kawamura, T. F. Stocker, High-resolution carbon dioxide concentration record 650,000–800,000 years before present. *Nature* **453**, 379–382 (2008).

39. K. L. Gwet, Computing inter-rater reliability and its variance in the presence of high agreement. *Br. J. Math. Stat. Psychol.* **61**, 29–48 (2008).

40. P. D. Sardeshmukh, B. J. Hoskins, The generation of global rotational flow by steady idealized tropical divergence. *J. Atmos. Sci.* **45**, 1228–1251 (1988).

41. M. Löfverström, J. M. Lora, Abrupt regime shifts in the North Atlantic atmospheric circulation over the last deglaciation. *Geophys. Res. Lett.* **44**, 8047–8055 (2017).

42. M. Löfverström, R. Caballero, J. Nilsson, G. Messori, Stationary wave reflection as a mechanism for zonalizing the Atlantic winter jet at the LGM. *J. Atmos. Sci.* **73**, 3329–3342 (2016).

43. J. L. Oster, W. D. Sharp, A. K. Covey, J. Gibson, B. Rogers, H. Mix, Climate response to the 8.2 ka event in coastal California. *Sci. Rep.* **7**, 3886 (2017).

44. M. Kirby, J. Barbosa, J. Carlin, G. MacDonald, J. Leidelmeijer, N. Bonuso, J. Han, B. Nauman, J. Avila, A. Woodward, S. Obarr, C. Poulsen, K. Nichols, R. Ramezan, Holocene hydroclimatic variability recorded in sediments from Maddox Lake (northern California Coast Range). *Quat. Res.* **115**, 90–108 (2023).

45. X. Liu, P. Chang, D. Fu, R. Saravanan, H. Wang, N. Rosenbloom, S. Zhang, L. Wu, Improved simulations of atmospheric river climatology and variability in high-resolution CESM. *J. Adv. Model. Earth Syst.* **14**, e2022MS003081 (2022).

46. F. Pöppelmeier, A. Jeltsch-Thömmes, J. Lippold, F. Joos, T. F. Stocker, Multi-proxy constraints on Atlantic circulation dynamics since the last ice age. *Nat. Geosci.* **16**, 349–356 (2023).

47. V. L. Peck, I. R. Hall, R. Zahn, H. Elderfield, F. Grousset, S. R. Hemming, J. D. Scourse, High resolution evidence for linkages between NW European ice sheet instability and atlantic meridional overturning circulation. *Earth Planet. Sci. Lett.* **243**, 476–488 (2006).

48. S. Toucanne, G. Soulet, N. Freslon, R. S. Jacinto, B. Dennielou, S. Zaragosi, F. Eynaud, J.-F. Bourillet, G. Bayon, Millennial-scale fluctuations of the European Ice Sheet at the end of the last glacial, and their potential impact on global climate. *Quat. Sci. Rev.* **123**, 113–133 (2015).

49. D. A. Hodell, J. A. Nicholl, T. R. R. Bontognali, S. Danino, J. Dorador, J. A. Dowdeswell, J. Einsle, H. Kuhlmann, B. Martrat, M. J. Mleneck-Vautravers, F. J. Rodríguez-Tovar, U. Röhl, Anatomy of Heinrich Layer 1 and its role in the last deglaciation. *Paleoceanogr. Paleoclimatol.* **32**, 284–303 (2017).

50. D. J. Thornalley, D. W. Oppo, P. Ortega, J. I. Robson, C. M. Brierley, R. Davis, I. R. Hall, P. Moffa-Sanchez, N. L. Rose, P. T. Spooner, I. Yashayaev, L. D. Keigwin, Anomalously weak Labrador Sea convection and Atlantic overturning during the past 150 years. *Nature* **556**, 227–230 (2018).

51. C. Zhu, Z. Liu, Weakening Atlantic overturning circulation causes South Atlantic salinity pile-up. *Nat. Clim. Change* **10**, 998–1003 (2020).

52. L. Caesar, G. D. McCarthy, D. J. R. Thornalley, N. Cahill, S. Rahmstorf, Current atlantic meridional overturning circulation weakest in last millennium. *Nat. Geosci.* **14**, 118–120 (2021).

53. B. Orihuela-Pinto, M. H. England, A. S. Taschetto, Interbasin and interhemispheric impacts of a collapsed atlantic overturning circulation. *Nat. Clim. Change* **12**, 558–565 (2022).

54. W. Liu, A. V. Fedorov, S.-P. Xie, S. Hu, Climate impacts of a weakened atlantic meridional overturning circulation in a warming climate. *Sci. Adv.* **6**, eaaz4876 (2020).

55. J. W. Hurrell, M. M. Holland, P. R. Gent, S. Ghan, J. E. Kay, P. J. Kushner, J.-F. Lamarque, W. G. Large, K. Lindsay, W. H. Lipscomb, M. C. Long, N. Mahowald, D. R. Marsh, R. B. Neale, P. Rash, S. Vavrus, M. Vertenstein, D. Bader, W. D. Collins, J. J. Hack, J. Kiehl, S. Marshall, the community earth system model: A framework for collaborative research. *Bull. Am. Meteorol. Soc.* **94**, 1339–1360 (2013).

56. R. B. Neale, Description of the NCAR Community Atmosphere Model (CAM 5.0), NCAR Tech. Note Sci. and Tech. Rep, NCAR/TN486+STR (NCAR Publication Office, Boulder, CO, 2010).

57. J. Nusbaumer, T. E. Wong, C. Bardeen, D. Noone, Evaluating hydrological processes in the Community Atmosphere Model Version 5 (CAM5) using stable isotope ratios of water. *J. Adv. Model. Earth Syst.* **9**, 949–977 (2017).

58. T. E. Wong, J. Nusbaumer, D. C. Noone, Evaluation of modeled land-atmosphere exchanges with a comprehensive water isotope fractionation scheme in version 4 of the Community Land Model. *J. Adv. Model. Earth Syst.* **9**, 978–1001 (2017).

59. M. Kageyama, S. Albani, P. Braconnot, S. P. Harrison, P. O. Hopcroft, R. F. Ivanovic, F. Lambert, O. Marti, W. R. Peltier, J.-Y. Peterschmitt, D. M. Roche, L. Tarasov, X. Zhang, E. C. Brady, A. M. Haywood, A. N. LeGrande, D. J. Lunt, N. M. Mahowald, U. Mikolajewicz, K. H. Nisancioglu, B. L. Otto-Bleisner, H. Renssen, R. A. Tomas, Q. Zhang, A. Abe-Ouchi, P. J. Bartlein, J. Cao, Q. Li, G. Lohmann, R. Ohgaito, X. Shi, E. Volodin, K. Yoshida, X. Zhang, W. Zheng, The PMIP4 contribution to CMIP6 – Part 4: Scientific objectives and experimental design of the PMIP4-CMIP6 last glacial maximum experiments and PMIP4 sensitivity experiments. *Geosci. Model Dev.* **10**, 4035–4055 (2017).

60. W. R. Peltier, D. F. Argus, R. Drummond, Space geodesy constrains ice age terminal deglaciation: The global ICE-6G_C (VM5a) model. *J. Geophys. Res. Solid Earth* **120**, 450–487 (2015).

61. S. Menemenlis, J. M. Lora, M. Lofverstrom, D. Chandan, Influence of stationary waves on mid-Pliocene atmospheric rivers and hydroclimate. *Global Planet. Change* **204**, 103557 (2021).

62. C. B. Skinner, J. M. Lora, C. Tabor, J. Zhu, Atmospheric river contributions to ice sheet hydroclimate at the last glacial maximum. *Geophys. Res. Lett.* **50**, e2022GL101750 (2023).

63. S. H. Baek, J. M. Battalio, J. M. Lora, Atmospheric river variability over the last millennium driven by annular modes. *A. G. U. Adv.* **4**, e2022AV000834 (2023).

64. J. M. Lora, C. A. Shields, J. J. Rutz, Consensus and disagreement in atmospheric river detection: ARTMIP global catalogues. *Geophys. Res. Lett.* **47**, e2020GL089302 (2020).

65. J. J. Rutz, C. A. Shields, J. M. Lora, A. E. Payne, B. Guan, P. Ullrich, T. O'Brien, L. R. Leung, F. M. Ralph, M. Wehner, S. Brands, A. Collow, N. Goldenson, I. Gorodetskaya, H. Griffith, K. Kashinath, B. Kawzenuk, H. Krishnan, V. Kurlin, D. Lavers, G. Magnusdottir, K. C. Sarangi, S. Sellars, T. Shulgina, R. Tome, D. Waliser, D. Walton, G. Wick, A. M. Wilson, M. Viale, The atmospheric river tracking method intercomparison project (ARTMIP): Quantifying uncertainties in atmospheric river climatology. *J. Geophys. Res. Atmos.* **124**, 13777–13802 (2019).

66. W. S. Broecker, D. McGee, K. D. Adams, H. Cheng, R. L. Edwards, C. G. Oviatt, J. Quade, A great basin-wide dry episode during the first half of the mystery interval? *Quat. Sci. Rev.* **28**, 2557–2563 (2009).

67. J. L. Conroy, C. Karamperidou, D. A. Grimley, W. R. Guenthner, Surface winds across eastern and midcontinental North America during the last glacial maximum: A new data-model assessment. *Quat. Sci. Rev.* **220**, 14–29 (2019).

68. R. Feng, T. Bhattacharya, B. L. Otto-Bleisner, E. C. Brady, A. M. Haywood, J. C. Tindall, S. J. Hunter, A. Abe-Ouchi, W.-L. Chan, M. Kageyama, C. Contoux, C. Guo, X. Li, G. Lohmann, C. Stepanek, N. Tan, Q. Zhang, Z. Zhang, Z. Han, C. J. R. Williams, D. J. Lunt, H. J. Dowsett, D. Chandan, W. R. Peltier, Past terrestrial hydroclimate sensitivity controlled by Earth system feedbacks. *Nat. Commun.* **13**, 1306 (2022).

69. C. B. de Wet, D. E. Ibarra, B. K. Belanger, J. L. Oster, North American hydroclimate during past warms states: A proxy compilation-model comparison for the Last Interglacial and the Mid-Holocene. *Paleoceanogr. Paleoclimatol.* **38**, e2022PA004528 (2022).

70. J. L. Oster, S. I. Macarewich, M. Lofverstrom, C. de Wet, I. Montañez, J. M. Lora, C. Skinner, C. Tabor, North Atlantic meltwater during Heinrich Stadial 1 drives wetter climate with more atmospheric rivers in western North America (2023).

71. J. S. Munroe, B. J. C. Laabs, Latest Pleistocene history of pluvial Lake Franklin, northeastern Nevada, USA. *G. S. A. Bull.* **125**, 322–342 (2013).